In situ investigation of spinodal decomposition in hypermonotectic Al–Bi and Al–Bi–Zn alloys

New Journal of Physics
The open-access journal for physics

In situ investigation of spinodal decomposition in hypermonotectic Al–Bi and Al–Bi–Zn alloys

P L Schaffer[1,5], R H Mathiesen[2], L Arnberg[1], M Di Sabatino[3] and A Snigirev[4]

[1] Department of Materials Science and Technology, Norwegian University of Science and Technology, N-7491 Trondheim, Norway
[2] Department of Physics, Norwegian University of Science and Technology, N-7491 Trondheim, Norway
[3] SINTEF, Materials and Chemistry, N-7465 Trondheim, Norway
[4] Experiments Division, European Synchrotron Radiation Facility, F-38043 Grenoble, France
E-mail: paul.schaffer@material.ntnu.no

New Journal of Physics **10** (2008) 053001 (16pp)
Received 16 February 2008
Published 6 May 2008
Online at http://www.njp.org/
doi:10.1088/1367-2630/10/5/053001

Abstract. Spinodal decomposition of hypermonotectic Al–6 wt.%Bi, Al–8 wt.%Bi and Al–6 wt.%Bi–8 wt.%Zn alloys has been investigated using synchrotron radiography. In the case of the 6 and 8 wt.%Bi binary alloys undercoolings of 70 and 110 K, respectively, were required to initiate the $L \rightarrow L_1 + L_2$ reaction, which appeared to occur very close to the monotectic reaction temperature. The nucleated L_2 droplets were set in collective size-dependent motion by forces coupled to external fields (gravity and imposed temperature gradient) as well as forces arising due to internal fluctuations of the system. With experimental conditions similar to those realized during strip casting of the same materials, it was found that the size-dependant droplet velocity field combined with Stokes drag at the L_1–L_2 interfaces as well as attractive and repulsive diffusion-coupling between adjacent L_2 droplets, yield complex meso- to microscale hydrodynamics. The hydrodynamics are the dominating mechanisms for L_2 droplet coagulation, and are accordingly decisive for the final size distribution and geometrical dispersion of the soft Bi-rich component in the cast material. A different decomposition mode was observed in the Al–6 wt.%Bi–8 wt.%Zn ternary alloy, with the L_2 droplets undergoing an immiscible–miscible–immiscible transition. In contrast to what

[5] Author to whom any correspondence should be addressed.

was found for the binaries, L_2 domains formed at relatively small undercoolings, and very little droplet motion was observed, as all L_2 domains nucleated and remained on the crucible walls until they encroached on the monotectic front. At small distances from the monotectic front a Zn-rich solute boundary layer preceding the α-Al, caused the L_2 domains to dissolve as Bi–Zn–Al regains complete miscibility upon reaching a critical Zn-concentration. In the shallow mush region behind the monotectic reaction, a high Zn solid solubility and a relatively fast diffusion of Zn in α-Al combine to cause a rapid diminishing Zn concentration in the mush liquid, restoring Bi-immiscibility and consequentially a secondary nucleation of L_2 droplets in the mush.

Contents

1. Introduction

Aluminium-based hypermonotectic alloys are of particular interest due to the unique microstructures that form during solidification and they have been identified as candidate materials for engine bearings. Amongst several candidates, hypermonotectic Al–Bi alloys appear to be well suited, combining an ideal volume fraction of homogeneously distributed soft Bi-rich second phase particles with a lower melting temperature, within an Al-rich light weight hardenable matrix that can resist high pulsating loads, giving good overall tribological properties [1]. However, during casting a temperature range exists where the homogeneous Al–Bi liquid decomposes into two immiscible liquids with a large difference in density; Bi-rich droplets dispersed in an Al-rich liquid. This situation also applies to other Al-based hypermonotectics (Al–Pb and Al–In) and represents a serious challenge to the various industrial processing steps involved as gravity-induced macrosegregation and subsequent coalescence of the denser minority phase is practically impossible to remedy, and has for the most part been considered a major obstacle for the design of suitable casting processes for hypermonotectic bearings.

Interestingly, experiments under micro-gravity conditions investigating Al–Pb and Al–Pb–Bi alloys have shown that at significant temperature gradients a thermo-capillary motion (so-called Marangoni motion) of the minority phase droplets is induced [2, 3]. This means that under terrestrial conditions, an adequately large and directional temperature gradient acting

anti-parallel to gravity during casting will induce thermo-capillary motion of the minority phase droplets and could potentially be utilized to counteract gravity induced settlement. This principle has, in fact, been partially realized through the development of a vertical strip casting process for production of hypermonotectics suitable for bearings [4]. However, the key variables influencing liquid–liquid phase separation and subsequent microstructure development are not completely clear and therefore, the process is far from optimized.

In the past, micro-focused x-rays have been employed to study structure formations in immiscible metallic liquids *in situ* by radiographic imaging [5, 6]. Using conventional sources, the spatiotemporal resolutions obtained were of the order of 20–30 μm at several seconds exposure per frame, limiting the application of this method to studies of stationary melt structures and slow coarsening processes at the solid–liquid boundaries in the mushy zone. More recently, *in situ* x-ray imaging microscopy of solidification phenomena has been carried out with micrometre spatial and sub-second temporal resolutions by exploiting the high brilliance offered by synchrotron radiation sources [7]. The proximity to full video-microscopic resolutions opens the way for studies of the dynamics of liquid–liquid phase separation and the current work reports on the first use of *in situ* synchrotron x-ray video microscopy to observe Al–Bi and Al–Bi–Zn alloys during directional solidification, under conditions that should be reasonably analogous to the vertical strip casting process [4].

2. Theoretical background

The phase diagram for the Al–Bi system can be seen in figure 1. At hypermonotectic compositions (i.e. > 3.4 wt.%Bi) the components form a liquid phase, L, which is completely miscible above the binodal temperature, $T_{\mathrm{bin}}(c_0)$, where c_0 is the nominal Bi concentration. At a certain undercooling below $T_{\mathrm{bin}}(c_0)$, L decomposes into two immiscible liquids, $L \rightarrow L_1 + L_2$, where Bi-rich L_2 droplets nucleate and grow by diffusion in the Al-rich L_1 matrix melt until the monotectic temperature, T_{mon}, is reached. The region of the phase diagram between $T_{\mathrm{bin}}(c_0)$ and T_{mon} is known as the *liquid two-phase zone* (*LTPZ*). Upon further cooling below T_{mon}, the monotectic reaction, $L_1 \rightarrow \alpha$-Al + L_2 occurs. Finally, Bi solidifies by the reaction $L_2 \rightarrow \alpha$-Al + Bi at T_{Bi}.

Herein, we will be concerned mainly with the *LTPZ* for which the solid–liquid interface formed during the monotectic reaction can be regarded as its low-temperature boundary. Assuming equilibrium conditions, the length of the *LTPZ*, l_{LTPZ}, can be expressed by c_0 and the imposed temperature gradient, ∇T, as:

$$l_{\mathrm{LTPZ}} = \frac{T_{\mathrm{bin}}(c_{\mathrm{o}}) - T_{\mathrm{mon}}}{\nabla T}. \tag{1}$$

In practice, however, liquid–liquid phase separation will occur under non-equilibrium conditions restricted by the transport of heat and mass to and from the constituent phases and the exterior heat sinks. Heat diffusion in liquid metals is usually several orders of magnitude faster than its chemical counterpart, and can, therefore, be regarded as complete at the micro- to mesoscopic length scales relevant to this study. Consequentially, local thermodynamic equilibrium applies at the L_1–L_2 interfaces. Mass and momentum are conserved by the system, as given by Wu *et al* [9]:

$$\sum_{j=1}^{2} \sum_{i \neq j} \frac{\partial}{\partial t}(f_i \rho_i) + \nabla \cdot (f_i \rho_i \mathbf{u}_i) - M_{ji} = 0, \tag{2}$$

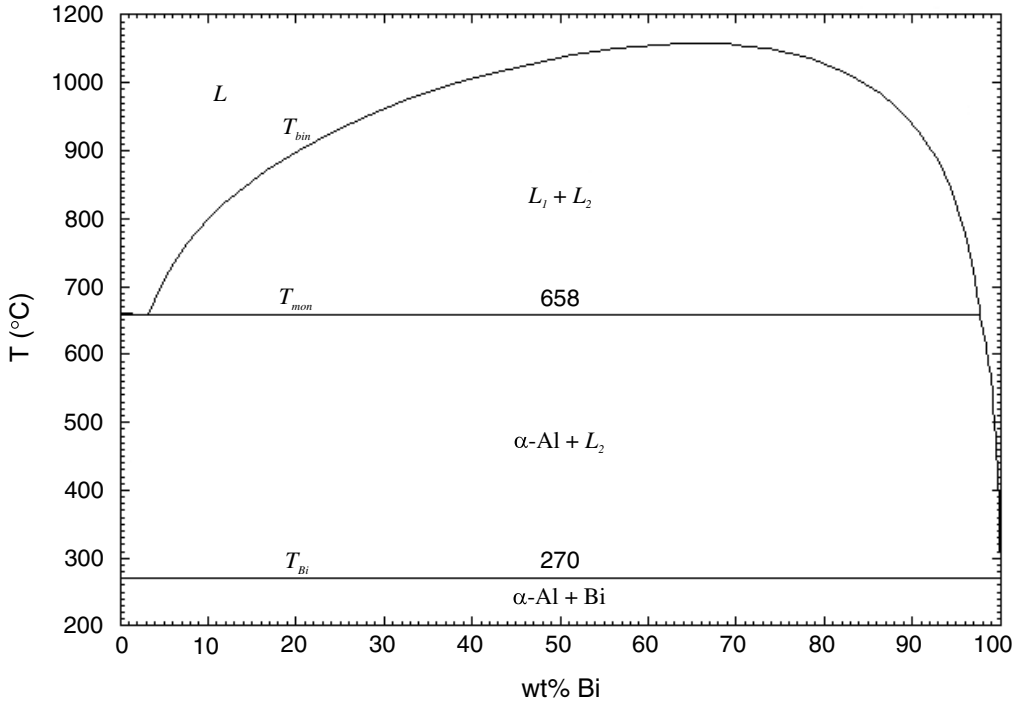

Figure 1. Al–Bi phase diagram. Adapted from [8].

$$\sum_{j=1}^{2}\sum_{i\neq j}\frac{\partial}{\partial t}(f_i\rho_i\mathbf{u}_i)+\nabla\cdot(f_i\rho_i\mathbf{u}_i\otimes\mathbf{u}_i)+f_i\nabla p-\nabla\overline{\overline{\tau_i}}-f_i\rho_i\boldsymbol{g}-\mathbf{U}_{ji}-\mathbf{F}_{\mathrm{M}}=0, \tag{3}$$

where the sums are taken over the two constituent phases L_1 and L_2 with $\otimes$ as the diadic product, $f_1 + f_2 = 1$ and ρ_i are the phase specific volume fractions and densities, respectively. $\mathbf{u}_i$ is the velocity vector, p the hydrostatic pressure, τ_i a stress–strain tensor, $\boldsymbol{g}$ is gravity, M_{ji} and $\mathbf{U}_{ji}$ are the mass and momentum exchange terms respectively, and $\mathbf{F}_{\mathrm{M}}$ is the volume averaged Marangoni force.

Under the assumption that no pre-existing liquid momentum is transferred from the miscible liquid region at $T > T_{\mathrm{bin}}(c_0)$ into the two-phase liquid state, any subsequent flow must develop in the *LTPZ*. In that case (3) can be rephrased to an initial equation of motion for a single spherical L_2 droplet of radius R under the following force balance:

$$\rho R^3\frac{\mathrm{d}\mathbf{u}}{\mathrm{d}t}=\Delta\rho R^3\mathbf{g}+6\eta_1\frac{2\eta_1+3\eta}{\eta_1+\eta}R\Delta\mathbf{u}+\frac{3R^2\eta_1}{(\eta_1+\eta)}\left[\frac{\kappa_1}{2\kappa_1+\kappa}\frac{\partial\sigma}{\partial T}\nabla T+\frac{D_1}{(2D_1+D)}\frac{\partial\sigma}{\partial c}\nabla c\right]$$
$$=F_{\mathrm{g}}(R)+F_{\mathrm{S}}(R)+F_{\mathrm{M}}(R,T,c), \tag{4}$$

where the index $i = 2$ corresponding to the second phase L_2 has been omitted. Here, $\Delta\rho = \rho_2 - \rho_1$, η the dynamic viscosities for the two liquid phases, $\Delta\mathbf{u} = \mathbf{u}_1 - \mathbf{u}$ the velocity of the L_1 liquid relative to the droplet velocity, κ the thermal conductivities of the liquids, σ the L_1–L_2 interfacial energy, and D the mass diffusion coefficients of the liquids. Equation (4) is derived under the assumption that droplets are small enough for mass- and heat diffusion to be complete at any time inside the droplets, and may be further simplified to a first approximation assuming uniform transport properties in the two liquid phases, i.e. $\kappa = \kappa_1$ and $D = D_1$. The

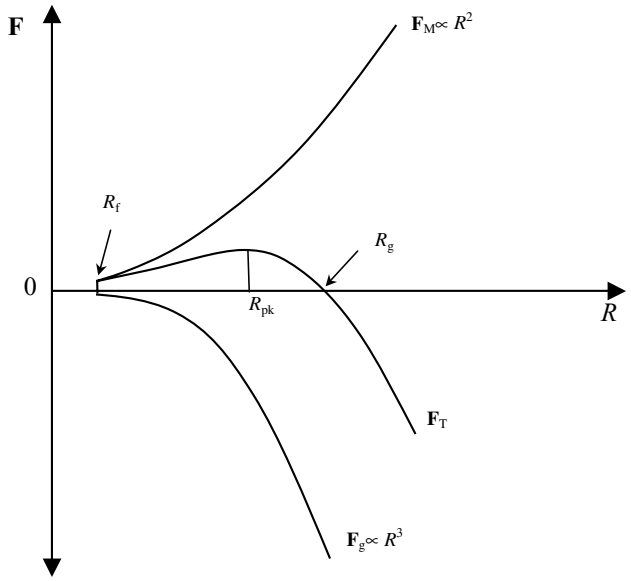

Figure 2. Schematic representation of the R-dependence of $\mathbf{F}_M$ and $\mathbf{F}_g$.

three force terms on the rhs of (4) relate to gravity, Stokes friction and thermosolutal-capillarity (Marangoni), respectively.

Upon cooling below the binodal line, meta-stable embryos/clusters of L_2 form by homogeneous nucleation and fluctuate in size and shape until they reach the required nucleation undercooling where they form droplets of a critical radius R_n. The droplets will be instantaneously exposed to a force field, but may not be set in motion before they reach a size, R_f, where the acting forces are large enough to overcome Stokes friction. Provided that the thermosolutal-capillarity is strong enough relative to the viscosities, droplets may eventually enter into a size regime where $\mathbf{F}_M > \mathbf{F}_g + \mathbf{F}_S$. It should be noted that in (4), $\mathbf{F}_M$ is comprised of a thermal and solutal term and as the Bi concentration in L_1 increases with temperature in the *LTPZ* (i.e. follows the binodal line) the solutal Marangoni force also acts in the same direction as ∇T. Consequentially, with ∇T anti-parallel to $\boldsymbol{g}$, $\mathbf{F}_M$ opposes $\mathbf{F}_g$. The two acting forces scale with the droplet surface area and volume, respectively (see (4)) and their sum gives the total force, $\mathbf{F}_T$. As long as $R_f < R < R_g$, with R_g as the critical radius where $\mathbf{F}_g = \mathbf{F}_M$, the net force on the droplet remains positive and there will be a droplet motion $\mathbf{u}$ anti-parallel to $\boldsymbol{g}$ as shown in figure 2. By careful control of ∇T, L_2 droplet sedimentation may be counterbalanced, making it feasible to solidify hypermonotectic alloys with a homogeneous distribution of the Bi-rich phase.

However, equation (4) only accounts for the motion of isolated non-interacting droplets. Obviously, the size-dependent force terms lead to a variety of individual motions as soon as any droplet size distribution is introduced. Thus, for a collective ensemble of droplets, motion will be along different trajectories and with different net velocities, for which droplet–droplet interactions will become critical. Evidently other terms, not accounted for in (4) must be introduced. Primarily this concerns attractive and repulsive force terms between interacting droplets and micro- to mesoscopic hydrodynamic force fields that arise in the *LTPZ* as a result of the collective droplet motions and droplet–droplet interactions. Tanaka [10] has shown that in a system containing a high droplet density, coupling of the diffusion fields between

droplets occurs, leading to an attractive or repulsive force. The *diffusion-coupling mechanism* is mainly of relevance in the absence of melt flow where droplet coalescence occurs on the diffusive time and length scales. In the presence of melt flow, Tegze *et al* [11] have shown that hydrodynamically driven coalescence is several orders of magnitude faster than the diffusion-coupling mechanism. In general there are at least seven mechanisms that can contribute to droplet coalescence or repulsion, although for the most specific cases only a selection of these mechanisms will be of practical relevance since their inherent dynamics are posed on different scales. The specific coalescence mechanisms that apply in this study will be discussed in the results section.

Droplet motion and interactions in the *LTPZ* of hypermonotectic systems are inherently complex to handle from a modelling perspective, as the fundamental mechanisms driving motion and interaction act over several orders of magnitude in both length and time. For example, the microstructure development model by Wu *et al* [9] only investigates L_2 transport on a macroscopic scale and does not include any criteria for coalescence of the L_2 phase, which later will be shown to be extremely important with respect to the final size distribution of the L_2 phase. In addition, this model does not include any of the diffusion controlled mechanisms for droplet motion. On the other hand, phase field modelling by Tegze *et al* [11] is on a comparatively very short time and length scale, micrometre (μm) and microsecond (μs), far too small to incorporate the effects of meso- and macroscopic flow that occur over the length of the *LTPZ*. Therefore, the important hydrodynamic forces that determine droplet motion are not well described on typical casting length and timescales and to date have not been successfully modelled.

3. Experimental

Castings with nominal compositions of Al–6 wt.%Bi, 8 wt.%Bi and Al–6 wt.%Bi–8 wt.%Zn were prepared by melting 99.999% purity Al, Bi and Zn in a clay graphite crucible coated with fibrefrax. When molten, the alloy was poured into an insulated bottom chilled mould, and after solidification sectioned to discard regions approximately 10 mm from the chill. Slices were then taken from the remainder of the casting perpendicular to the growth direction measuring $22 \times 11\,\mathrm{mm}^2$, and each slice was polished down to a final thickness of 140–160 μm before being coated with boron nitride and enclosed between the two 150 μm thick quartz glass plates. A Bridgman furnace was used for directional solidification of the thin samples with operating temperatures up to 1200 K [12]. The furnace allowed x-ray monitoring of the microstructure evolution in a fixed field of view with directional solidification possible parallel or antiparallel to $\boldsymbol{g}$.

The experiments were carried out at beam lines ID22 and BM05 at the European Synchrotron Radiation Facility (ESRF). The incident x-ray beam was monochromatized at 17 keV and the beam size applied gave a field of view corresponding to $1.3 \times 1.3\,\mathrm{mm}^2$. A detector capable of fast acquisition of high resolution images was used to obtain nominal spatial and temporal resolutions of 1.5 μm and 0.15 s, respectively. More details on the source, detector together with a description of fundamental aspects of x-ray transmission imaging with respect to x-ray interactions with matter can be found elsewhere [12].

Samples were placed in the furnace and melted in one of two ways; either with the sample in contact with the hot and cold zone such that the monotectic front was stabilized in the field of view (L_2 droplets pushing/engulfment experiments) or with the entire sample in the hot zone of

the furnace where it was held until it was completely molten (all other experiments). Samples were then translated with a constant pulling or pushing velocity, $\mathbf{v}_{sp}$ ∇T was varied between 2.5 and 30 K mm^{-1} and $|\mathbf{v}_{sp}|$ from 3.5 to 17.5 μm s^{-1}.

4. Results and discussion

4.1. Binary alloys

Several solidification sequences will be presented here showing the various microstructures that develop depending on ∇T and ∇c, and will be discussed in the context of the hydrodynamic forces described in section 2.

4.1.1. Low temperature gradient. Figure 3 shows three frames from video sequence 1 (available from stacks.iop.org/NJP/10/053001/mmedia), where a binary Al–8 wt.%Bi alloy was solidified at $\nabla T = 2.5\,\mathrm{K\,mm^{-1}}$ and $\mathbf{v}_{sp} = 3.5\,\mu\mathrm{m\,s^{-1}}$. These images highlight the important stages of phase separation and microstructural evolution at what is considered a low ∇T. At $t =$ 0 several Bi-rich droplets with $R \sim 1\,\mu$m have nucleated in the Al-rich liquid (circles at $t = 0$). Although it appears that the Bi-rich droplets nucleate in a position clearly ahead of the monotectic front, as the sequence continues (at $t = 3.5$ and 7.0 s) it becomes apparent that two α-Al grains have also nucleated and are growing in the same location as the initial L_2 nucleation at $t = 0$. It would be expected that α-Al grains are also present at $t = 0$ as homogeneous nucleation of L_2 would be highly unlikely when thermodynamically favourable nucleating surfaces, such as α-Al, are present.

Interestingly, despite the alloy having a hypermonotectic composition, nucleation of L_2 occurs concurrently with the α-Al during the monotectic reaction $L_1 \rightarrow \alpha\text{-Al} + L_2$ and no immiscible liquid forms directly as described by the reaction $L \rightarrow L_1 + L_2$, implying that L_2 nucleation occurs at high undercoolings, namely $T_{bin}(c_0) - T_{mon} \sim 70$ and 110 K for $c_0 = 6$ and 8 wt.%Bi respectively, both considerably above what has been used in modelling, where nucleation of L_2 is assumed to homogeneously nucleate at relatively moderate undercoolings (20 K for a $c_0 = 10$ wt.%Bi alloy) [9]. Due to the resolution limit of this imaging technique, the minimum observable L_2 droplet size, R_{min}, was $\sim 1\,\mu$m and it should be noted that smaller L_2 droplets below this size could nucleate in the *LTPZ* at some distance ahead of the monotectic front. These droplets will have a radius $R_n < R < R_{min}$ and will experience forces proportional to R as described by (4) where they will either remain motionless due to viscous damping (i.e. $R < R_f$) or set in motion by thermo-capillary forces (i.e. $R_f < R < R_{min}$), moving parallel to ∇T. If present, L_2 droplets with $R_f < R < R_{min}$ will move with a velocity increasing with R, eventually causing larger droplets to overrun and collide with smaller ones, coalesce and form droplets with $R > R_g$ which would settle in the *LTPZ* from positions well ahead of the monotectic front. However, during a total of 33 solidification sequences with the binary alloys in the low ∇T regime, no L_2 droplets were observed to settle from higher temperature regions outside the field of view, supporting the conclusion that nucleation of the $L \rightarrow L_1 + L_2$ reaction was severely hindered. The conclusion is further supported by the fact that in the low ∇T regime, the complete liquid volume remains within the *LTPZ* as soon as ∇T has been established, leaving the system with several minutes for deep-in *LTPZ* coagulation to occur. Employing (1), l_{LTPZ} for the case shown in figure 1 is $\sim$44 mm, i.e. well beyond the full sample length.

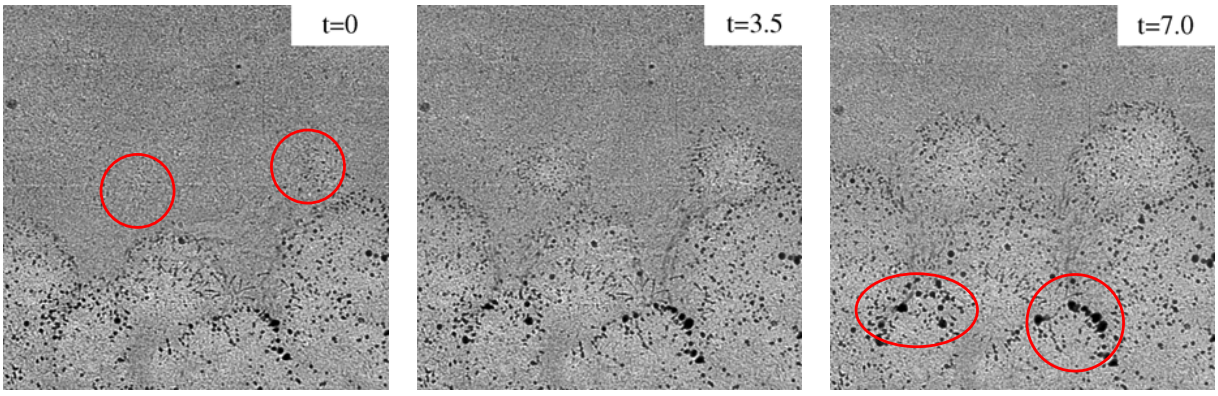

Figure 3. Al–8 wt.%Bi alloy solidified at $\nabla T = 2.5\,\mathrm{K\,mm^{-1}}$ and $\mathbf{v}_{sp} = 3.5\,\mu\mathrm{m\,s^{-1}}$. Bi-rich droplets are highlighted by circles at $t = 0\,\mathrm{s}$ and begin to settle due to gravity. At $t = 3.5\,\mathrm{s}$, equiaxed grains appear to be growing in the same location as the initial L_2 nucleation. Image size corresponds to $1.3 \times 1.3\,\mathrm{mm^2}$.

As the monotectic reaction progresses, α-Al forms an equiaxed structure and Bi-rich droplets can be seen to settle by gravity due to the relatively low thermosolutal-capillarity induced with this ∇T. The open equiaxed network allows Bi-rich droplets to settle relatively freely and they accumulate on top of α-Al grains (highlighted by circles at $t = 7.0\,\mathrm{s}$) where the network becomes more constricted. Bi-rich droplets can be seen to coarsen by agglomeration in the open network, driven by a reduction of the total L_1–L_2 interfacial energy of the system, equivalent to an Oswald ripening process. At higher α-Al solid fractions Bi-rich droplets become trapped in the α-Al equiaxed network, remaining in the liquid state until T_{Bi} is reached.

4.1.2. Intermediate temperature gradient. At intermediate ∇T's, a large number of L_2 droplets are set in motion by thermosolutal Marangoni forces giving rise to convective and shear flows on both microscopic and mesoscopic scales with prominent hydrodynamically driven droplet–droplet interactions and coalescence in the *LTPZ*. The complex droplet motion and coalescence can be observed ahead of the monotectic front in video sequence 2 (available from stacks.iop.org/NJP/10/053001/mmedia) where solidification takes place at $\nabla T = 14.6\,\mathrm{K\,mm^{-1}}$ and $\mathbf{v}_{sp} = 3.5\,\mu\mathrm{m\,s^{-1}}$. A striking difference to the low ∇T experiment is the increased complexity required to describe the droplet motions.

Although the exact location of L_2 droplet nucleation is difficult to ascertain due to the dynamic nature of liquid–liquid phase separation, it can be assumed that nucleation occurs on the monotectic front as in the low ∇T experiment. Once nucleation occurs, L_2 droplets grow by diffusion leading to short range Bi concentration variations in L_1 and when $R > R_f$, they will be set in motion by the forces described in (4).

With the increased ∇T, a buoyant movement of L_2 droplets is initiated by a dominant Marangoni-contribution and droplets will move away from the monotectic front permitting further nucleation events to occur in their wake. However, comparing with theory, R_g from the experiments is at least 50 times larger than that corresponding to pure thermo-capillarity Marangoni case which is often used when modelling hypermonotectic phase separation [9, 11].

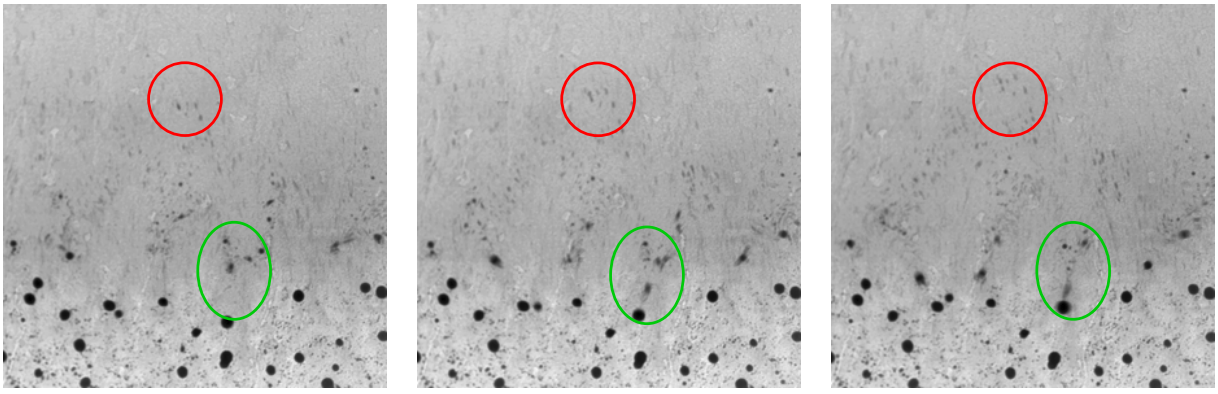

Figure 4. Al–6%Bi alloy solidified at $\nabla T = 14.6\,\mathrm{K\,mm^{-1}}$ and $\mathbf{v}_{sp} = 3.5\,\mu\mathrm{m\,s^{-1}}$. Small droplets are transported anti-parallel to $\boldsymbol{g}$ by Marangoni motion (red circles) whereas large droplets settle due to $\boldsymbol{g}$ (green circles). Image size corresponds to $1.3 \times 1.3\,\mathrm{mm^2}$ and $\Delta t_{img} = 0.25\,\mathrm{s}$.

Presumably this deviation can be ascribed to: the presence of a strong solutal Marangoni contribution, the L_2 phase nucleating on small α-Al crystals freely suspended in the undercooled melt or a combination of the two. The first case arises due to the lack of potent L_2 nucleation sites in the *LTPZ* and subsequently all L_2 nucleation occurs in the vicinity of/on the monotectic front, leading to significant Bi-concentration fluctuations in the L_1 in this region. Assuming local equilibrium to apply at the L_1–L_2 interface, even a modest concentration gradient would correspond to a large temperature difference resulting in a strong soutal-capillarity contribution to $\mathbf{F}_M$. In the second case, small potent α-Al grains may nucleate ahead of an undercooled monotectic reaction or arise from detachment at the monotectic front. Nucleation and growth of L_2 on these grains could result in the formation of a L_2 droplet containing an α-Al core, subsequently reducing the $\mathbf{F}_g$ term in (4).

Figure 4 shows three consecutive frames from video sequence 2 with $\Delta t_{img} = 0.25\,\mathrm{s}$ (where $\Delta t_{img} = \Delta t_{exposure} + \Delta t_{readout}$) where L_2 droplets are both rising (red circles) and settling (green circles) reflecting the ∇T and R dependent balance between $\mathbf{F}_g$ and $\mathbf{F}_M$. Image processing of the complete sequence reveals that L_2 droplets with $R > 5\,\mu\mathrm{m}$ are located within $\Delta T_{L_2} = T - T_{mon} < 5.1\,\mathrm{K}$, corresponding a distance $< 350\,\mu\mathrm{m}$ ahead of the monotectic front, and the smaller droplets that have escaped beyond this region, predominantly move anti-parallel to $\boldsymbol{g}$. For droplets $R < 5\,\mu\mathrm{m}$ remaining $< 350\,\mu\mathrm{m}$ from the monotectic front, the situation is more complex since these could either escape or be involved in the many coagulation events that occur in this region.

L_2 droplets with a radius R_f to R_g, will move through the *LTPZ* by Marangoni motion toward higher temperatures with $\mathbf{u} \propto R$, during which they will either dissolve as a consequence of the increase in Bi-solubility in L_1, or increase in size by collisions with other L_2 droplets moving at different velocities and become super critical in size (i.e. $R > R_g$) and subsequently settle. Assuming thermodynamic equilibrium to apply for the mass transport across the L_1–L_2 interfaces during the L_2 droplet dissolution process, complete internal mixing of L_2 inside the droplet would be just as fast as the droplet motion itself due to the Marangoni flow inside the droplet and the relatively small droplet size. Accordingly, droplet dissolution should occur quite close to full thermodynamic equilibrium. Therefore, L_2 droplets should only completely

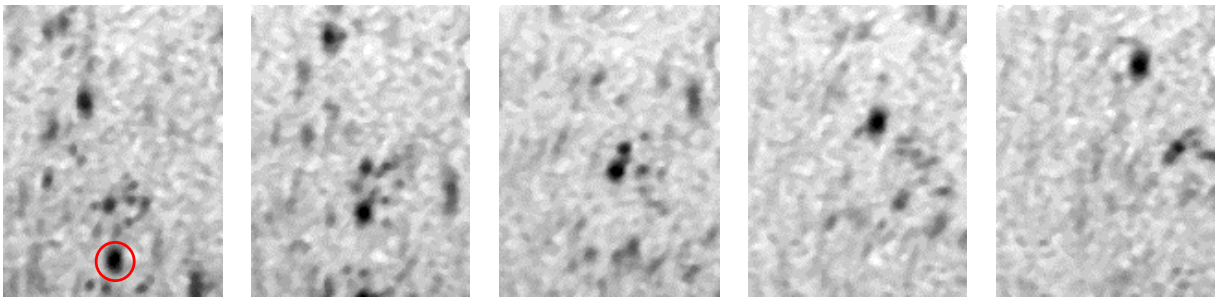

Figure 5. Five consecutive images showing Marangoni-induced droplet coalescence. The large droplet (highlighted by the circle) moves anti-parallel to gravity, during which smaller, slower moving droplets, are intercepted. Image size corresponds to $0.16 \times 0.22\,\mathrm{mm}^2$ and $\Delta t_{\mathrm{img}} = 0.25\,\mathrm{s}$.

dissolve after being transported into the miscible region (i.e. $T > T_{\mathrm{bin}}$) where the surface tension between L_1 and L_2 effectively reduces to zero. This would result in a local enrichment of Bi causing an unstable density layering, from which the heavier Bi-rich liquid would start to settle. The density layering settlement combined with the uprising Marangoni motion would subsequently lead to the formation of natural convection rolls on a mesoscopic scale, with a diameter similar to l_{LTPZ}. For the images shown in figure 4, that corresponds to a roll diameter of $\sim$5 mm or 3.8 times the field of view.

As stated above, not all droplets in the size regime R_{f} to R_{g} are expected to move out of the *LTPZ* and dissolve. Since $\mathbf{u} \propto R$, larger droplets will tend to overrun smaller ones, colliding leading to Marangoni-motion-induced coalescence. This is demonstrated in figure 5, where a large droplet (circled) overruns smaller, slower moving droplets, leading to coalescence.

Droplets undergoing consecutive collisions by this mechanism would eventually become super critical and start settling towards the monotectic front. Consequently, two opposing flows arise locally, and as shown by Gruber–Pretzler *et al* [13], the shear flow zones give rise to the formation of unstable vortices in the *LTPZ*; however the size of the vortices as determined by the two-phase volume average model of Gruber–Pretzler is larger by a factor of $\sim$3.7 compared to the average size found from the experiment shown in video sequence 2. This discrepancy can, most likely, be ascribed to the fact that the Gruber–Pretzler model does not incorporate droplet coagulation, leaving L_2 droplet growth to occur by diffusion only. Obviously, L_2 droplet coagulation will result in droplets obtaining a radius $> R_{\mathrm{g}}$ much closer to the monotectic front than in the purely diffusive growth case, and from video sequence 2 droplet coagulation can be observed as prominent features at the high-temperature side for practically all the vortices formed.

In the zone where the opposing flows shear, catastrophic collision induced coalescence events occur, an example of which can be seen in figure 6, where a large settling droplet (circle) impacts with a stream of smaller uprising droplets. Also note, in this sequence, how Stokes drag from the colliding droplets sets up a local hydrodynamic field that serves to transport other adjacent droplets towards the collision centre in the wake of the first droplet–droplet impact.

The large settling droplets finally come to rest at the monotectic front where they continue to coarsen by further coagulation and local diffusion of Bi from the adjacent L_1 liquid. By diffusive growth each droplet will be surrounded by a Bi-depleted L_1 layer. Hence, a repulsive

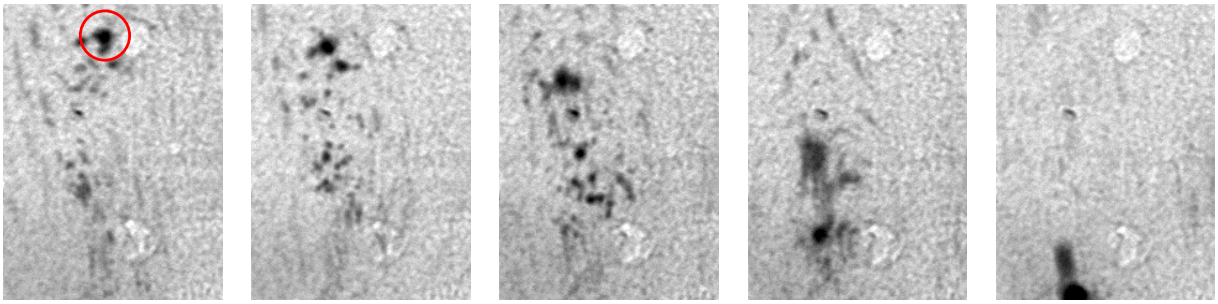

Figure 6. Five consecutive images showing an example of Stokes-induced droplet coalescence, where the largest droplet (highlighted by the circle) can be seen to collide with smaller uprising droplets. Image size corresponds to $0.24 \times 0.33\,\mathrm{mm}^2$ and $\Delta t_{\mathrm{img}} = 0.25\,\mathrm{s}$.

diffusion coupling [10] arises between the large droplets resting on the interface, causing them to attain a semi-periodic distribution at the monotectic front (see figure 4). Upon its progress, the monotectic front will have to push or engulf the L_2 droplets. The latter can only be achieved by allowing for a local perturbation of the growing α-Al front, causing a local undercooling of the monotectic reaction facilitating local enrichment and depletion of Bi ahead of the positive and negative curved features of the interface respectively.

The large L_2 droplets will come to rest at locations confining them to local minima in potential energy and during settlement to the regions of negative curvature, Bi-enriched L_1 will be dragged by Stokes flow into the wake of the settling L_2 droplets, leading to further coarsening. Furthermore, as soon as the monotectic front has attained these periodic perturbations, other L_2 droplets arriving at the positively curved interface by settlement, will cause further flow into the troughs, giving support to local microscale convection loops that can attain a periodicity similar to that of the monotectic front, as shown in figure 7 and video sequence 3 (available from stacks.iop.org/NJP/10/053001/mmedia). The loops may form ahead of the front due to the shear flow and droplet coagulation mechanisms described previously.

The shear that occurs between the neighbouring convection loops gives rise to massive coalescence events in the liquid just ahead of the monotectic reaction (highlighted by the arrows in figure 7). Presumably the sample confinement along the incident x-ray beam direction contributes to the establishment of such a semi-periodic quasi-stable convection regime, since in a non-confined geometry it would be reasonable to assume the microscopic flow caused by monotectic front perturbations and local L_2 droplet interaction mechanisms to attain rather non-regular geometries.

4.2. L_2 droplet coalescence mechanisms

The hydrodynamic flow fields described above operate on the meso- and meso-microscopic scale and result from the influence of external fields as well as from diffusion-coupling and repulsion [10]. However, local L_1 solute fluctuations and short range hydrodynamic forces, such as flow assisted coalescence [11] and Tanaka's 'collision-induced collision' mechanisms [14], will also have a significant impact on L_2 droplet coalescence.

In the region immediately ahead of the monotectic front, the L_1 liquid is super-saturated in Bi due to the suppressed L_2 nucleation described above, and the position of L_2 droplet

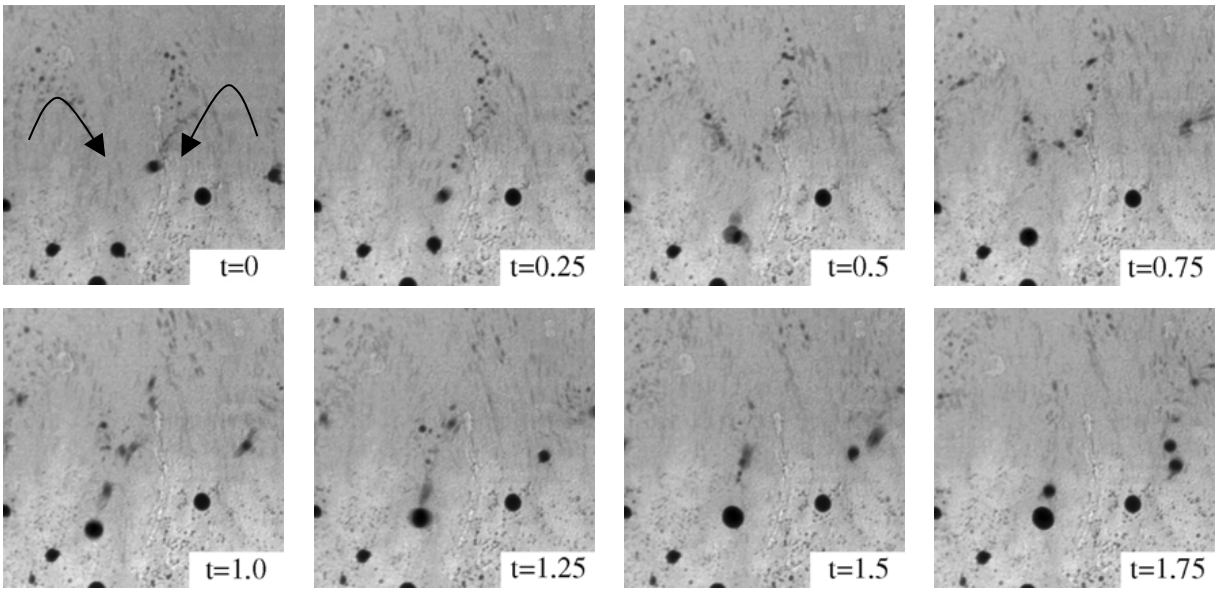

Figure 7. Microscale convection loop immediately ahead of the monotectic front. Arrows highlight the direction of L_2 droplet motion. Image size corresponds to $0.6 \times 0.6\,\mathrm{mm}^2$.

nucleation on the monotectic front will be transient as the location of the highest nucleation potency will shift with the evolving front. Consequently, local Bi fluctuations in L_1 will occur in this region, resulting in short range solute gradients and thus a strong multidirectional solutal-Marangoni effect. The L_2 droplets will therefore have many different trajectories, enhancing the likelihood of L_2 droplet interaction and collision near the monotectic front.

The hydrodynamic forces such as diffusion-coupling and flow assisted coalescence, although likely to be present, are difficult to examine due to the spatial and temporal resolution limits and the superimposed coarse scale hydrodynamic flow fields. However, Tanaka's collision-induced collision mechanism [14] was observed. This mechanism occurs due to the flow field generated by shape relaxation when two L_2 droplets coalesce and surrounding L_2 droplets in close proximity to the positively curved interfaces are drawn towards the collision centre and subsequently coalesce, while L_2 droplets close to the negatively curved interfaces are repelled from the collision centre. An example of collision induced collision is shown in figure 8, where two large L_2 droplets (labelled 1 and 2) move towards each other and subsequently collide resulting in the attraction of small L_2 droplets located near the positively curved interfaces (i.e. left and right of L_2 droplets 1 and 2) and repulsion of small L_2 droplets located near the negatively curved interface (circles). The coalescence process can be seen more clearly in video sequence 4, available from stacks.iop.org/NJP/10/053001/mmedia.

It should be noted that in Tanaka's model [14] flow caused by L_2 droplet motion prior to the collision is not accounted for and only the flow induced by shape relaxation is considered. However, the motion of L_2 droplets 1 and 2 towards each other is rapid enough for their trailing wake to attract smaller L_2 droplets towards the collision centre prior to coalescence at $t = 0.5\,\mathrm{s}$. The flow due to L_2 droplet motion prior to coalescence will also significantly contribute to the collision rate. From the example shown in figure 8, it becomes apparent that although the hydrodynamic flow fields operating on the longer length and timescales tend to dominate the

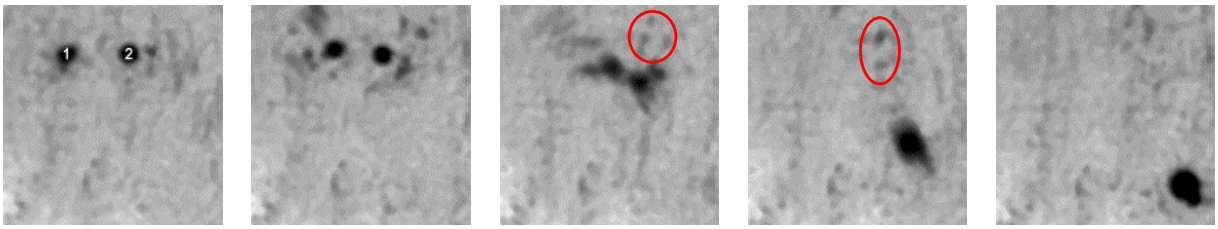

Figure 8. L_2 droplets 1 and 2 move together and coalesce and consequently draw smaller L_2 droplets towards them which also coalesce, after which they settle due to an increase in radius which is greater than R_g. Image size corresponds to $0.22 \times 0.22\,\mathrm{mm}^2$ and $\Delta t_{\mathrm{img}} = 0.25\,\mathrm{s}$.

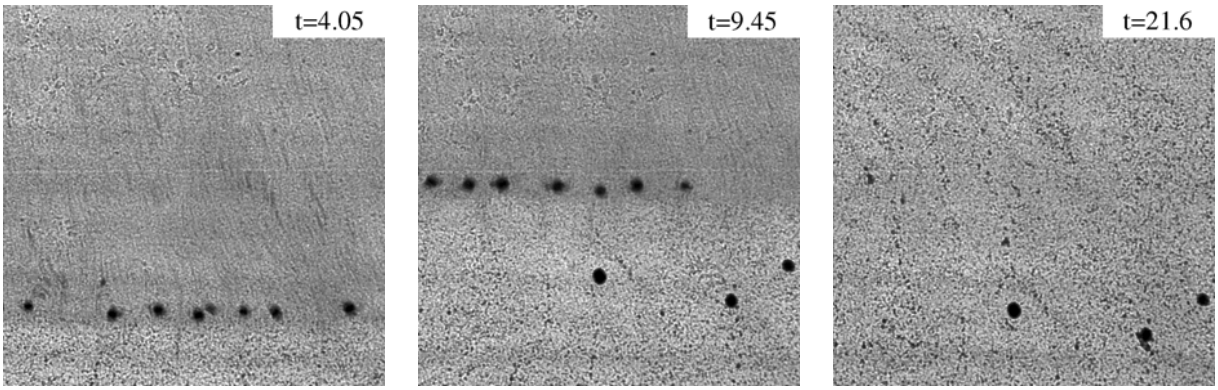

Figure 9. Al–8 wt.%Bi alloy solidified at $\nabla T = 16\,\mathrm{K\,mm}^{-1}$ and $\mathbf{v}_{\mathrm{sp}} = 10.5\,\mu\mathrm{m\,s}^{-1}$. L_2 droplet motion is predominantly anti-parallel to $\boldsymbol{g}$ due to the greater Marangoni force (seen as dark streaks) however larger L_2 droplets are located on the monotectic front. Image size corresponds to $1.3 \times 1.3\,\mathrm{mm}^2$.

overall L_2 droplet motion, short range hydrodynamics can be of major importance locally and therefore decisive to the final L_2 droplet size and dispersion.

4.3. Particle engulfment/pushing

Figure 9 shows three images from a sequence solidified at $\nabla T = 16\,\mathrm{K\,mm}^{-1}$ and $\mathbf{v}_{\mathrm{sp}} = 10.5\,\mu\mathrm{m\,s}^{-1}$ and the complete solidification sequence is shown in video sequence 5 (available from stacks.iop.org/NJP/10/053001/mmedia). In this sequence, a planar monotectic front was established in the field of view with the $\nabla T = 16\,\mathrm{K\,mm}^{-1}$ temperature gradient imposed prior to initiation of the sample pulling, in order to allow for a study of the collective pushing/engulfment dynamics at the planar front. The L_2 droplet motion is seen to be driven predominantly by Marangoni forces with droplets moving $||\nabla T$ appearing as dark streaks. Although not possible to resolve properly due to the high droplet velocities and spatio-temporal resolution limits, L_2 droplet–droplet interactions such as those found for the previous sequence would be expected to eventually arise. However, since the relatively short sequence shows a sample pulled with a semi-equilibrated monotectic front in the field of view, it only represents highly transient initial conditions.

The larger L_2 droplets rest on the monotectic front, where they initially coarsen by coalescence and local diffusion of Bi from the adjacent L_1. The latter eventually leads to Bi-depleted L_1-regions surrounding each of the L_2 droplets, with a repulsive diffusion-coupling [8] between neighbouring droplets as a result. With $D_1 = 1.1 \times 10^{-8}\,\mathrm{m^2\,s^{-1}}$ [9] and an average interface propagation velocity over the full sequence of $\sim 8.4 \times 10^{-5}\,\mathrm{m\,s^{-1}}$, where sample pulling is taken into account, the diffusion lengths involved are typically of the order of 1.3×10^{-4} m. This agrees reasonably well with an average droplet–droplet 150 μm separation measured directly from the images of the sequence. Although a few of the larger L_2 droplets become engulfed, the general trend is that they are pushed by the advancing interface. On the other hand, a substantial amount of smaller droplets are engulfed, clearly evident in the solid regions of the images.

Pushing of the large L_2 droplets and engulfment of smaller ones at the monotectic front is in contradiction with models used to describe particle pushing [15]. These models typically suggest the lower critical growth velocity for engulfment, $\mathbf{u}_{\mathrm{cr}}$, as being proportional to $1/R^x$, with $x = 1$–3, indicating larger particles to be more easily engulfed at the planar interface than smaller ones, since the former require less energy in terms of interface curvature. Although these models apply only for the pushing of solid particles, the L_2 droplets may be regarded to a first approximation, as soft particles due to the L_1–L_2 surface tension and the substantial difference in dynamic viscosities between the two constituent liquid phases.

An obvious explanation for this discrepancy may be that the particle pushing/engulfment relationships typically consider the interaction between the progressing interface and single non-interacting individual particles, and do not take into account either particle–particle interactions or situations where the particle dispersion is of the same order as the diffusive lengths controlling the interface propagation. Furthermore, as discussed previously the 'soft particle' droplets interact with each other and the parent melt (coagulation and attractive/repulsive diffusion coupling) via mechanisms that would not apply to a case with fully solid particles. Although locally a higher Gibbs energy is introduced by the perturbation during engulfment of smaller L_2 droplets, these events will occur at relatively large distances from one another, whereas engulfment of large droplets dispersed within the typical L_1 diffusion length would require perturbation of the entire interface, and consequentially cost more in terms of energy.

4.4. Ternary alloys

In the ternary system, a different liquid–liquid phase separation path was noted with L_2 nucleation occurring at modest undercoolings far ahead of the monotectic front. However, active nucleation sites were exclusively on the interior surfaces of the sample, i.e. no free nucleation of L_2 droplets in the melt was observed. Presumably the difference in nucleation behaviour with respect to the binary alloys can be ascribed to a difference in wetting conditions between the Bi-rich phase and the different oxides that form on the Al–Bi–Zn and Al–Bi samples.

The effect of the Zn addition can be observed in figure 10, where the irregular shaped dark phases are the L_2 droplets that have nucleated on the sample surface and move solely by the sample pulling as shown in video sequence 6 (available from stacks.iop.org/NJP/10/053001/mmedia). As the monotectic front (highlighted by red lines from $t = 16.8$–33.6 s) approaches the L_2 domains, they dissolve and form diffuse Bi-enriched clouds. The Bi–Zn binary system, which is also monotectic, has complete miscibility above 900 K, and the binodal transition temperature reduces even further with addition of Al. When the

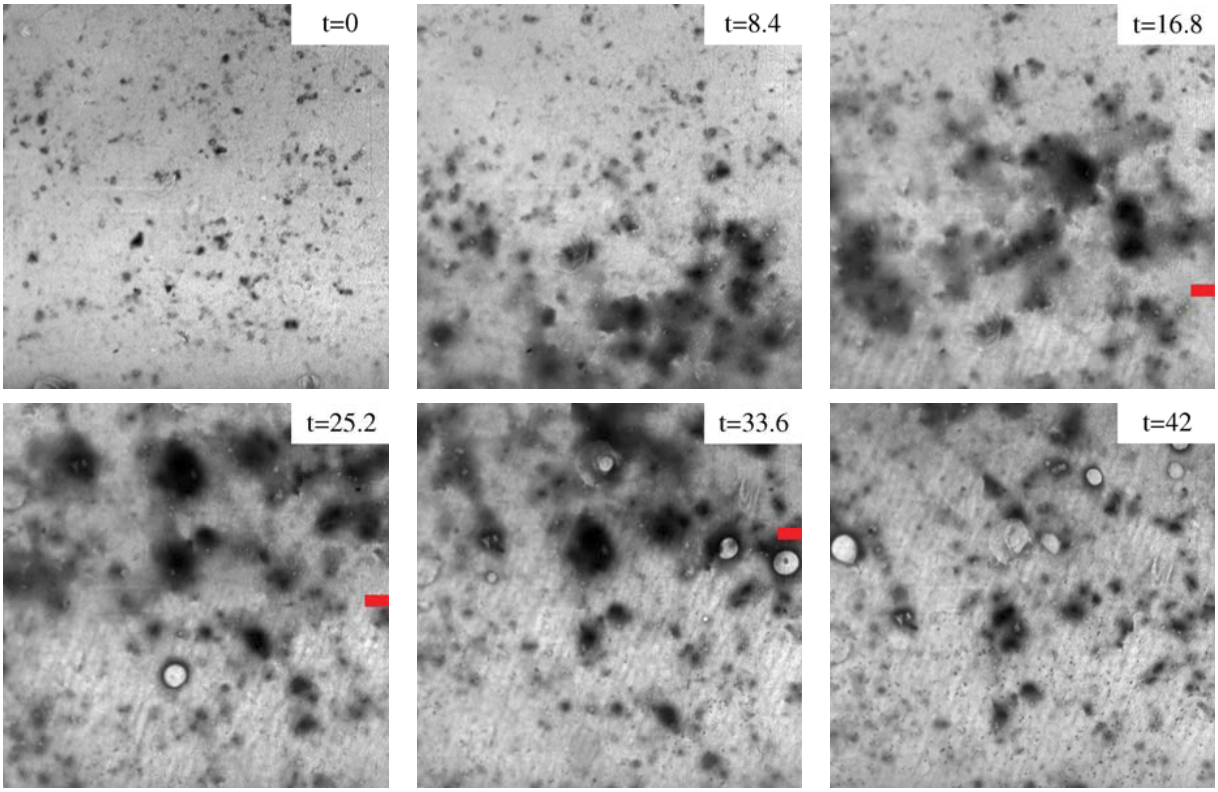

Figure 10. Al–6 wt.%Bi–8 wt.%Zn alloy solidified at $\nabla T = 60\,\mathrm{K\,mm^{-1}}$ and $\mathbf{v}_{sp} = 17.5\,\mu\mathrm{m\,s^{-1}}$. The transition from immiscible to miscible liquid when the Zn-rich boundary layer approaches can be seen from $t = 0$ to 16.8 s. As the diffuse Bi domains move closer to the monotectic front Zn concentration reduces and immiscibility re-establishes leading to secondary nucleation of L_2 droplets ($t = 25.2$ to 42 s).

monotectic reaction takes place by the reaction $L_1 \rightarrow \alpha\text{-Al} + \mathrm{Bi} + \mathrm{Zn}$, Zn is rejected ahead of the monotectic front forming a Zn-rich boundary layer. Consequentially, upon reaching a critical Zn-concentration at approximately 750 μm from the monotectic front, L_2 droplet surface tension reduces considerably leading to an immiscible–miscible transition where the L_2 droplets dissolve forming diffuse Bi-rich clouds ($t = 8.4$–33.6 s). However, as the dissolution occurs adjacent to the propagating monotectic front there is insufficient time for Bi to diffuse completely from the dissolved L_2-droplet region and form a locally homogeneous temperature dependent Bi-concentration in the melt ahead of the monotectic front. Accordingly, some larger L_2 droplets are found in the solid as the remnants of diffuse Bi-rich clouds formed in the *LTPZ*. With a Zn solid solubility in α-Al of $\sim$35 wt.% at the monotectic reaction temperature, and a relatively fast Zn solid diffusion $\sim 2 \times 10^{-12}\,\mathrm{m^2\,s^{-1}}$, the liquid Zn-concentration diminishes quite rapidly behind the monotectic front, where Bi-immiscibility is quickly re-established, causing secondary nucleation of fine L_2 droplets in the shallow mush region.

As a result of this phenomenon, it may be possible with some adjustment to develop a casting process that takes advantage of the Zn-driven L_2 droplet dissolution, to arrive at a cast material with a uniform, fine-dispersion of Bi particles. However, several challenges will remain that must be solved. Ideally L_2-dissolution should occur sufficiently far ahead of the monotectic

front such that the L_2 droplets diffuse completely into a homogeneous concentration in the melt. In addition, it is also not yet clear if re-establishment of Bi immiscibility and subsequent local L_2 droplet interactions provides enough time for the mean L_2 droplets to grow to the ideal sizes ($\sim$2–5 μm).

5. Conclusions

In situ investigations have been carried out on Al–Bi and Al–Bi–Zn alloys where liquid–liquid phase separation and subsequent L_2 droplet motion and interactions accounting for local and mesoscopic hydrodynamics were observed. In the binary alloys, the required undercooling to initiate the $L \rightarrow L_1 + L_2$ reaction was shown to be much higher than suggested in the literature ($\sim$110 K for the Al–8%Bi alloy) occurring simultaneously with or very close to the monotectic reaction. At higher ∇Ts, L_2 droplets are set in collective motion by hydrodynamic forces coupled to external fields which dominate L_2 droplet motion and interaction on a mesoscopic scale. In addition, short range hydrodynamic forces such as diffusion field coupling, flow assisted coalescence [11] and Tanaka's 'collision-induced collision' mechanisms [14], have also been shown to play important roles in the L_2 droplet–droplet coalescence process.

The experiments involving the Al–Bi–Zn ternary alloys revealed a different liquid–liquid phase separation path where Bi-rich domains formed at much smaller undercoolings than the binary alloys. During cooling Bi-rich domains underwent an immiscible–miscible–immiscible reaction due to the presence of a Zn-rich boundary layer ahead of the monotectic front.

Acknowledgments

This work was undertaken as part of the ESA Monophas MAP. The European Synchrotron and Radiation Facility is acknowledged for academic beam time.

References

[1] Ratke L and Diefenbach S 1995 *Mater. Sci. Eng.* R **15** 263–347
[2] Fujii H, Kimura T, Kitaguchi H, Kumakura H and Togano K 1995 *J. Mater. Sci.* **30** 3429–34
[3] Ratke L and Korekt G 2000 *Z. Metallk.* **91** 919–27
[4] Moiseev J, Zak H, Palkowski H and Tonn B 2005 *Aluminium* **81** 92–7
[5] Kaukler W F and Rosenberger F 1994 *Metall. Mater. Trans.* A **25** 1775–7
[6] Curreri P A and Kaukler W F 1996 *Metall. Mater. Trans.* A **27** 801–8
[7] Mathiesen R H 1999 *Phys. Rev. Lett.* **83** 5062–5
[8] 1986 *Binary Alloy Phase Diagrams* vol 1, ed T B Massalski (Ohio: American Society of Metals)
[9] Wu M, Ludwig A and Ratke L 2003 *Metall. Mater. Trans.* A **34** 3009–19A
[10] Tanaka H 1995 *J. Chem. Phys.* **103** 2361–4
[11] Tegze G, Pusztai T and Granasy L 2005 *Mater. Sci. Eng.* A **413–414** 418–22
[12] Mathiesen R H, Arnberg L, Ramsoskar K, Weitkamp T, Rau C and Snigirev A 2002 *Metall. Mater. Trans.* B **33** 613–23B
[13] Gruber-Pretzler M, Konozy L, Mayer F, Wu M, Ludwig A, Mathiesen R H, Schaffer P L and Arnberg L 2007 A numerical study of the impact of gravity and Marangoni force on the droplet distribution of hypermonotectic Al-Bi alloys *SP 07: Proc. 5th Decennial Int. Conf. on Solidification Processing* (*Sheffield, UK, 23–25 July 2007*) ed H Jones (Sheffield, UK: University of Sheffield) pp 249–53
[14] Tanaka H 1996 *J. Chem. Phys.* **105** 10099–1114
[15] Rohatgi P K, Yarandi F M, Liu Y and Asthana R 1991 *Mater. Sci. Eng.* A **147** L1–6